2004

Experimental validation of a smart-bias active magnetic bearing controller

Shailesh Pradhananga
Louisiana State University and Agricultural and Mechanical College, spradh1@lsu.edu

EXPERIMENTAL VALIDATION OF A SMART-BIAS ACTIVE MAGNETIC BEARING CONTROLLER

A Thesis
Submitted to The Graduate Faculty of the
Louisiana State University and
Agricultural and Mechanical College
In partial fulfillment of the
Requirements for the degree of
Master of Science in Mechanical Engineering

In

The Department of Mechanical Engineering

By
Shailesh Pradhananga
B.S., Regional Institute of Technology, Jamshedpur, India, 1996
August, 2004

Acknowledgements

I will begin by thanking my major Professor Dr. Marcio de Queiroz for his kind guidance and support during the experiment and in successful compilation of this thesis. He has been an excellent teacher and mentor during my graduate studies.

I would also like to thank Dr. Yitshak Ram and Dr. Wanjung Wang for serving as members on my committee and extending their kind support and assistance.

Also I would like to extend my gratitude to my colleague Zhijun Cai, LSU faculty and staff, in particular Jim Layton of the ME shop, for their assistance during the construction and setup of the experiment.

Table of Contents

List of Tables

List of Figures

Abstract

Active magnetic bearings (AMBs) are being increasingly employed in the aerospace industry in a variety of devices including compressors, turbines, pumps, and flywheels. One application of great interest to future space missions is the Integrated Power and Attitude Control System (IPACS). The IPACS consists of an arrangement of flywheels that integrates the energy storage and attitude control functions into a single system; thereby, reducing the spacecraft mass, volume, launching cost, and maintenance.

Like any energy storage system, flywheels need to be operated with low power losses. AMBs are ideally suited for flywheels because they eliminate mechanical losses (friction). Nevertheless, AMBs are subject to electrical losses, which are proportional to the bias flux. We recently developed an innovative solution to the problem of AMB control with reduced electrical power losses. The controller incorporates a *smart*, time-varying bias flux that reduces power losses without affecting the rotor stabilization. The novelty of the smart-bias controller strongly motivated the pursuit of the next step in this research – *an experimental validation*. To that end, the objectives of this project were:

- Design and build an experimental AMB test rig.
- Conduct tests to validate the smart-bias controller and its power-loss reduction mechanism in comparison to a standard constant-bias AMB controller.

The experimental results show that the smart-bias controller clearly reduces the electrical power losses and energy dissipation of the AMB system in comparison to the constant-bias approach, without significantly affecting the stabilization performance. These results confirm, in a qualitative manner, the theoretical and numerical results obtained earlier.

Chapter 1 Introduction

1.1 Motivation

Active magnetic bearings (AMBs) are experiencing an increased use in many rotating machines as an alternative to conventional mechanical bearings (e.g., fluid film and rolling element bearings). An AMB provides a non-contact means of supporting a rotating shaft through an attractive magnetic levitation force. The magnetic force is generated/controlled by passing an electric current through a coil wound around a stator made of ferromagnetic material (i.e., an electromagnet). Figure 1.1 below shows a one degree-of-freedom (DOF) AMB. Due to the non-contact nature of the bearings and rotor, AMBs have the unique ability to suspend loads with no friction, allow the operation of rotors at higher speeds, and operate under environmental conditions that prohibit the use of lubricants. Furthermore, since AMBs can be actively controlled, they offer other advantages over mechanical bearings such as eliminating rotor vibration through active damping, adjusting the stiffness of the suspended load, compensating for rotor misalignment and changes in rotor speed, and providing an automatic rotor balancing capability.

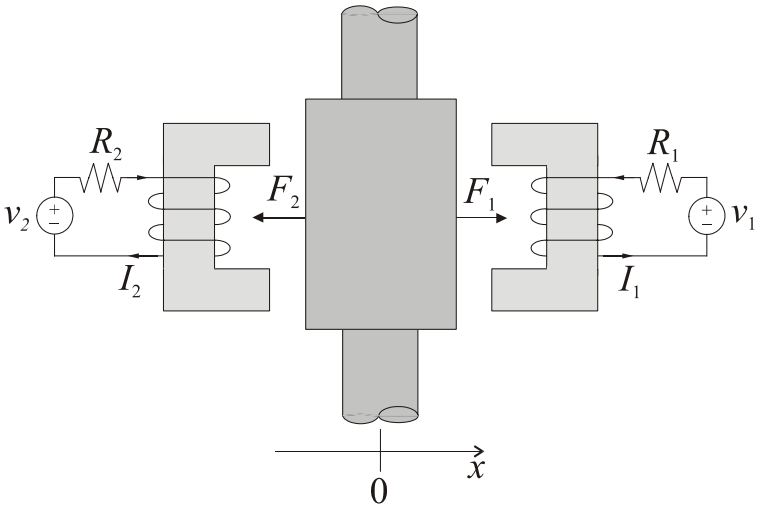

Figure 1.1: One-DOF AMB system

1.2 Space Applications

In the aerospace industry, AMBs are employed in a variety of devices including compressors, turbines, pumps, and flywheels. Among these devices, flywheels merit a more detailed discussion due to their importance to future space missions. A flywheel is an electromechanical battery that stores kinetic energy in a rotating disk for later use. Although the idea of utilizing a flywheel as an energy storage device is not new, there has been resurgence in flywheel technology motivated by the need to develop efficient, environmentally benign energy storage systems. Recent advances in high-strength, lightweight composite materials, AMBs, and power electronics have also propelled this interest. As a result, flywheels are now considered a viable alternative to other energy storage devices, such as chemical batteries, due to the following advantageous characteristics: i) no emissions or hazardous disposals, ii) high energy efficiency, iii) high specific power, iv) insensitivity to high rates of charge/discharge and depth of discharge, v) high lifetime cycle, and vi) operation at very high or low temperatures.

Flywheel systems have unique characteristics that make them well suited for applications that require a high level of energy and power management. One such application, which is of special interest to space technology, is called the Integrated Power and Attitude Control System (IPACS) [1]. Specifically, space vehicles currently utilize separate devices to provide energy storage and attitude control. Typically, the energy collected from solar arrays during periods of sunlight is stored in chemical batteries for use when the spacecraft is in the Earth's shadow. Attitude control is usually accomplished through an array of reaction wheels or control moment gyros. In contrast to this standard configuration, a suitable arrangement of four or more flywheels can integrate the energy storage and attitude control functions into a single system; thereby, reducing the spacecraft mass, volume, launching cost, and maintenance requirements. A

comprehensive literature review of the IPACS was presented in [4]. As noted in [4], the IPACS concept has been investigated since the 1970s [1]; however, the enabling technologies have only recently reached a level of maturity that facilitates on-board evaluation. In fact, the concept is currently under test by NASA and the Air Force Research Laboratory (AFRL) for use in the International Space Station [12] and other space missions.

1.3 AMB-Based Flywheels

The primary components of a flywheel system are the rotor, motor/generator, and bearings. The rotor is the component that effectively stores kinetic energy in the flywheel system, and is typically in the form of a disk or ring. The motor/generator is used to transfer energy to/from the flywheel by charging/discharging it. Specifically, the motor/generator uses incoming electric energy from the motor to spin up the rotor, and thereby, store kinetic energy. To draw energy from the flywheel, the process is reversed. That is, the rotor is slowed down to convert kinetic energy back into electric energy through the generator.

Since energy efficiency is one of the most important features of any energy storage system, flywheel systems need to be operated with very low mechanical and electrical power losses. The kinetic energy stored in a flywheel is given by $T = 1/2\, J\omega^2$ where J is the rotor moment of inertia about the axis of rotation and ω is the rotor angular speed. It is clear from this expression that to maximize the stored energy, the flywheel should be rotated at the highest speed allowed by the strength of the rotor material. AMBs are an ideal bearing candidate for flywheels due to their unique ability to suspend the rotor with no friction. This alleviates the problem of mechanical losses and hence, allows one to maximize the rotor speed. Nevertheless, AMBs are subject to electrical power losses as discussed in the following.

1.4 Electrical Power Losses in AMBs

Typically, an AMB is operated by introducing a high, fixed electrical current (or magnetic flux)[1] in each electromagnet, which referred to as the *bias current*. In the AMB, electrical current and magnetic flux are equivalent states of the system. This procedure facilitates the design of the AMB "control" current, which is superimposed on the bias current. Specifically, this conservative practice allows the system to be modeled by a controllable linear system; thus, enabling the application of standard linear control designs techniques [3], [9]. On the other hand, the bias current increases electrical power losses, which may cause rotor heating and affect the machine efficiency. That is, AMB electrical power losses are proportional to the current passing through the coils of the electromagnet (e.g., ohmic loss $\propto I^2$, rotating hysteresis loss $\propto I$, and eddy current loss $\propto I^2$ where I denotes the current [23]. While lowering or eliminating the bias current is desirable in order to minimize power losses, it enhances the AMB system nonlinearities and may lead to a control singularity (i.e., unbounded voltage control inputs) [14]. As is clear from this discussion, the design of AMB controllers that reduce electrical power losses is a theoretically challenging problem.

Fixed low-bias nonlinear controllers using the integrator backstepping technique [6] were proposed in [14, 16, 17] with no discussion about their implication on the AMB power losses. In [5], a gain-scheduled linear controller was developed with a low bias current. Low-bias control schemes were presented in [22, 21] using the small-gain theorem. Zero-bias control approaches were proposed in [2, 7, 20]. Unfortunately, these zero-bias results have the common drawback of potentially producing unbounded voltage control inputs. In [10], the first AMB control scheme based on the full-order, nonlinear system model that produces zero steady-state power losses and

[1] In the AMB, electrical current and magnetic flux are equivalent states of the system. Therefore, we will use these state variables interchangeably throughout the thesis for convenience.

no control singularity was proposed. The key to this result was the design of a bias flux in the form of an exponentially decaying function of time, which could be forced to zero at a slower rate than the regulation of the rotor position and velocity. Unfortunately, the result of [10] was theoretically restricted to controllers that ensure exponential stability of the closed-loop AMB system and hence, not applicable to cases of asymptotic or bounded stability that commonly occur with adaptive or robust controllers. Problems may also arise during practical implementation of the control strategy due to sensor noise and inaccuracy. These effects may cause the rotor position and velocity not to be zero in he steady state; however, the bias will still approach zero (due to its dependence on time possibly leading to a control singularity.

The above discussion indicates that the exponential-bias design proposed in [10] is a solution based on an idealized closed-loop AMB system. However, it provides an insight into its generalization to the more realistic scenario where sensor noise/inaccuracy are present and the stability result is not exponential. With this in mind, we were recently able to generalize the bias design of [10] by developing a *smart* bias flux [11]. The word "smart" was used to denote the fact that the bias varies on-line in a manner that reduces AMB power losses and avoids control singularities, without affecting the stability of the closed-loop system. This was accomplished by a novel design of the bias flux as a direct function of the rotor position and velocity. A numerical simulation in [11] successfully compared the performance of the proposed smart-bias controller with a standard constant-bias controller.

1.5 Research Objectives and Thesis Organization

The novelty, strength, and simplicity of the smart-bias AMB controller, as well as the encouraging numerical results presented in [11] strongly motivated the pursuit of the next step in this research – *an experimental validation*. To that end, the objectives of this project were:

- Design and build an experimental test rig that emulates the one-DOF AMB system shown in Figure 1.1.
- Conduct tests to evaluate the smart-bias controller in comparison to a standard constant-bias AMB controller in terms of stabilization performance, ohmic power losses, and energy dissipated.

This thesis is organized as follows. In Chapter 2, the experimental test rig is discussed. Detailed descriptions of the test rig components are presented. In Chapter 3, detail design and control development for smart bias is presented as also shown in [11]. A simple, specific expression for the bias function is presented satisfying the given conditions. In Chapter 4, the experimental procedure and results are discussed. A comparative study is made between the smart-bias and constant-bias controllers with respect to stabilization, power loss and energy dissipated. Finally, Chapter 5 includes overall conclusions for this work.

Chapter 2 Experimental AMB Test Rig

2.1 Overview

In order to experimentally evaluate the smart-bias controller, we first built an experimental test rig that emulates the one-DOF AMB system depicted in Figure 1.1. The test rig was inspired by the AMB system recently proposed as a nonlinear control benchmark experiment [8]. This benchmark experiment was a subject of two invited sessions in the 2000 American Control Conference [13]. The schematic drawing of the test rig is shown in Figure 2.1.

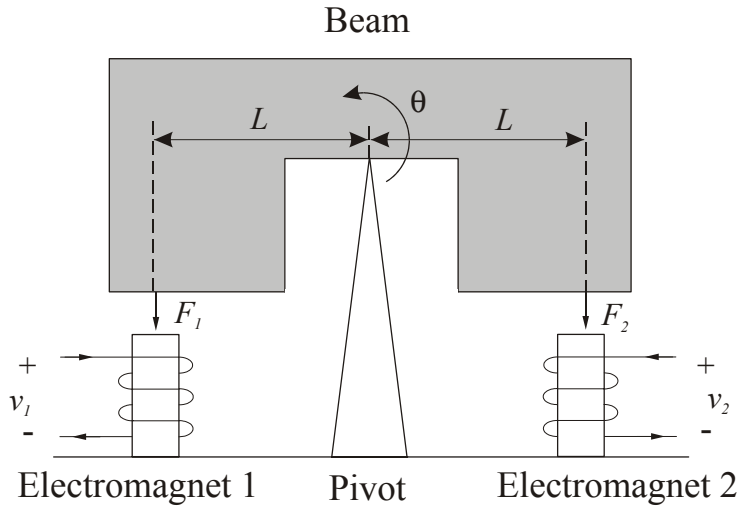

Figure 2.1: Schematic of the one-DOF AMB test rig

The test rig consists of a rigid beam that is free to rotate about a support pivot located at its center of mass. The angular position $\theta(t)$ of the beam is controlled by the two electromagnets fixed at the ends of the beam. Although having a simple mechanical construction this test rig incorporates all the typical nonlinearities of an AMB system. Specifically, since the weight of the beam is compensated by the pivot (i.e. no gravitational effects), the dynamic behavior of this system is analogous to the one axis of an AMB-supported flywheel in a spacecraft [8]. Hence, this system can act as an ideal test rig for evaluating AMB controllers aimed at space applications. The components of the AMB testbed can be divided into following three categories:

a. Mechanical and structural components;

b. Electromagnet components;

c. Electrical and electronic components.

A description of each category follows.

2.2 Mechanical and Structural Components

The mechanical and structural components of the test rig are shown in Figure 2.2. The specifications given in [8] were followed in the design and construction of these components. The main goals were to ensure [8]: (i) the beam center of mass was located at the pivot point, and (ii) the structure had a sufficiently high first natural frequency. The beam was made from 316 stainless steel, which has a relative permeability approximately equal to air. A ferromagnetic target made of silicon-iron alloy laminations was attached to the ends of the beam by the lamination brace to provide a permeable material for the AMBs to attract. Mechanical stops were placed on the inward clamps to prevent the beam from hitting and damaging the electromagnet iron cores.

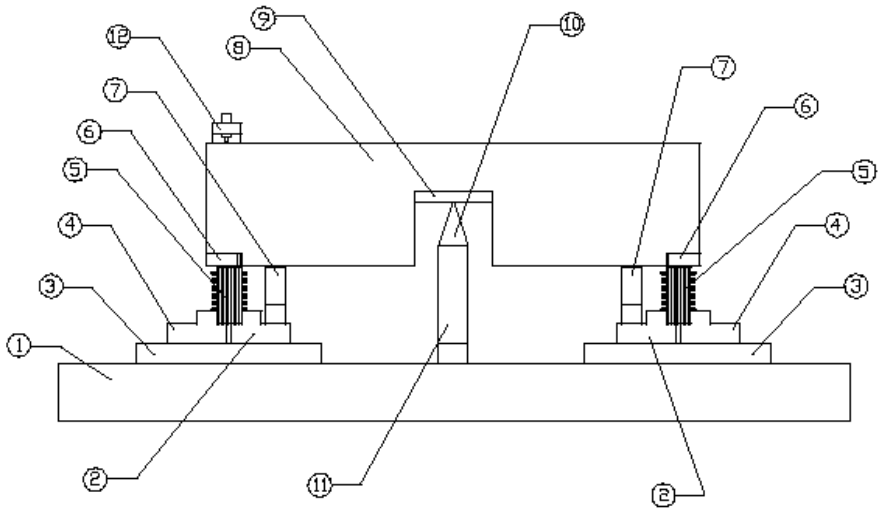

Figure 2.2: Mechanical and structural components (figure is a courtesy of Dr. Carl Knospe [8]).

Table 1.1: Legends for Figure 2.2

1. Base plate	7. Auxiliary stop
2. Inward clamp	8. Beam
3. Support plate	9. Balance plate
4. Outward clamp	10. Pivot
5. Electromagnet	11. Pivot support
6. Lamination brace	12. Sensor stand

2.3 Electromagnet Components

Each electromagnet is comprised of the iron core, bobbin, and coil. Each part is described in detail below.

Iron Core. Thomas & Skinner Inc. donated the Orthosil EI laminations for the electromagnet iron core and beam target piece. The use of laminations helps minimize eddy current effects in the electromagnet. Orthosil is an iron silicon alloy developed to provide low core losses. Each lamination has a thickness of 0.36 mm and was cleaned and glued together using Bond master (MAGNA-TAC E645) to make 42 stacks of laminations. MAGNA-TAC E645, which was donated by Beacon Chemicals, is a two-part thermosetting epoxy that exhibits fast penetration and strong metal-to-metal adhesion.

Bobbin. The bobbins were made from an aluminum sheet cut into rectangular pieces of the required dimension and glued together to give the final shape of the bobbin. The bobbin was made out of a solid aluminum piece to ensure high structural integrity. The bobbin has a rectangular groove so it fits over the center leg of the iron core.

Drive Coil. The drive coil for the electromagnet is a 22 AWG copper magnet wire with single build polyurethane nylon insulation, purchased from MWS Wire Industries. The wire was wrapped around the bobbin with 244 turns, and then fit around the iron core. The coil has a resistance of 1.3 Ω at room temperature.

2. 4 Electrical and Electronic Components

These components include the displacement and current sensors, power amplifiers, signal conditioning circuits, power supplies, data acquisition board, and computational control platform. Detail specifications of each are given below.

Displacement and Current Sensors. The beam angle was measured using a Bentley Nevada 3300 Proximity Transducer System. Its principle of operation is based on eddy current, and it requires a power supply of –17.5 Vdc to –26 Vdc for operation. The linear operating range of the sensor is 10 to 90 mils from the target. The displacement sensor is calibrated by placing shims of various thicknesses in the gap between the target and the electromagnet, and recording the corresponding output voltage. The increment in the shim thickness was 1 mil. The calibration curve is obtained as shown in Figure 2.3, indicating a sensor sensitivity of 1.27 mil/V.

The output voltage of the displacement sensor was applied to an A/D converter with input range of ± 10 V. In order to make full use of this range, the output of the displacement sensor was passed through an amplification and offset circuitry before sending it to A/D converter. The signal conditioning circuit was designed such that the sensor provides 0 V when the beam is perfectly balanced (i.e. $\theta = 0$) and approximately ± 10 V at the maximum and minimum displacements. The signal conditioning circuit is shown in Figure 2.4. The offset was adjusted through the potentiometer labeled R6 in the circuit diagram. The gain is the ratio of R2 and R1.

Current Sensor. The current sensor built in to the LPAM-1 power amplifier from Quanser was used to measure the coil current. The sensitivity of the sensor is 0.5 V/A, and it can measure a continuous (peak) current of 7 (9) A.

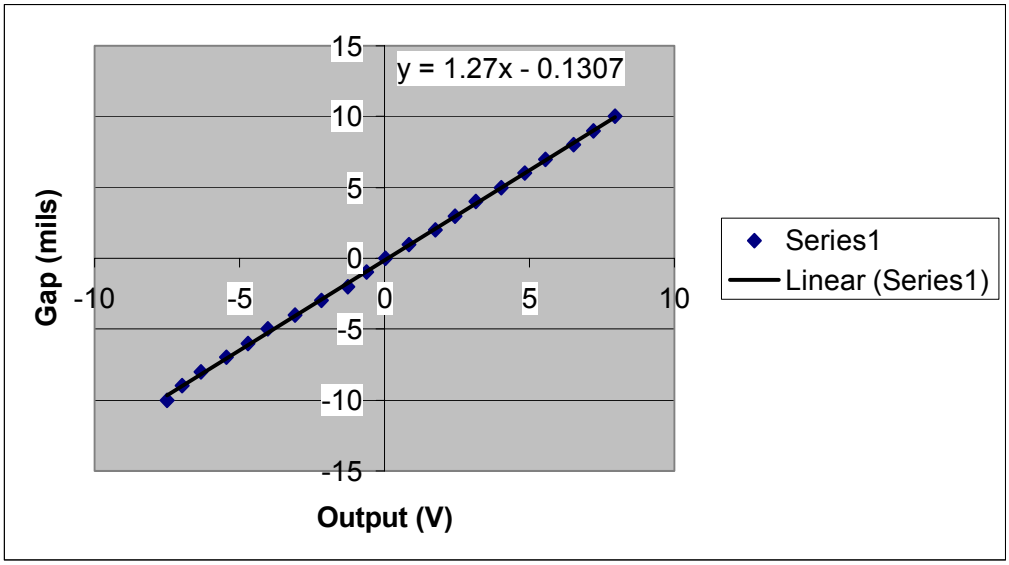

Figure 2.3: Calibration curve for displacement sensor

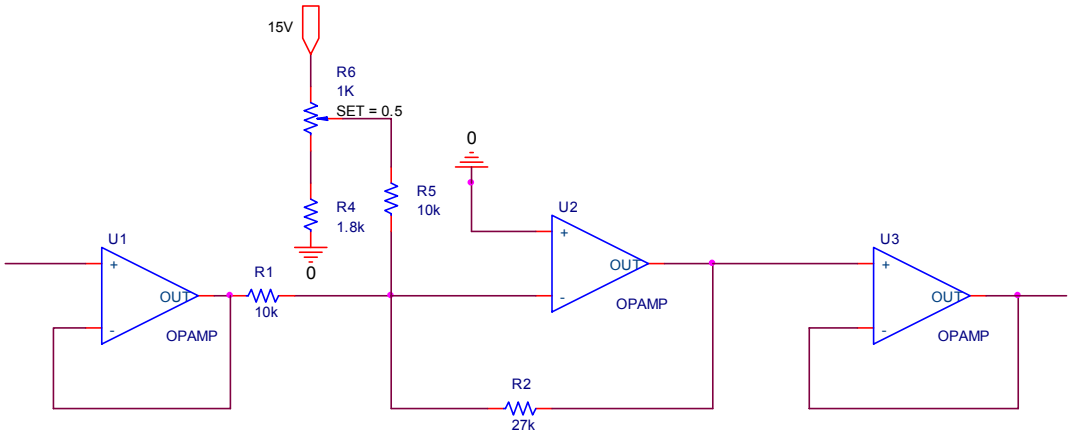

Figure 2.4: Signal conditioning circuit for displacement sensor

Power Amplifiers. Two linear power amplifier modules LPAM-1from Quanser are used to drive the electromagnet coils. The amplifier, which can be operated in either voltage or current, has a bandwidth of more than 10 kHz. The amplifiers were set to the voltage mode since the control inputs of the control scheme being tested are the voltages applied to the electromagnets. The amplifier output current is rated at 7A continuous and 9A peak. When the supply voltage is 48 V, the amplifier input voltage range is ± 20 V.

dSPACE System. The control algorithm was implemented on the dSPACE ACE kit 1104. This system provides all the hardware and software tools to execute control algorithms in real time. Specifically, the dSPACE ACE kit 1104 has three components: (i) Implementation Software Real-Time Interface (RTI), (ii) Single-Board Hardware DS1104 R & D Controller Board, and (iii) Experiment Software MLIB/MTRACE and Control Desk Standard. The control algorithm is initially modeled in Simulink. RTI, together with Mathworks' Real-Time Workshop, then generates the required real-time code from the Simulink model. The implementation software includes a C cross compiler for PowerPC processors, Assembler, and a linker. The inputs and outputs of the Simulink model are connected to the dSPACE I/O board by dragging and dropping the I/O module from the RTI block library, and then connecting it to the Simulink blocks. Once the model is implemented, it is run on the DS1104 Controller Board. The controller board is composed of a main processor (MPC8240, PowerPC 603e, 250 MHz), a slave DSP subsystem (Texas Instruments' DSP TMS320F240), and the I/O board. The comprehensive on-board I/O includes four 16-bit AD channels, four 12-bit AD channels, eight 16-bit DA channels, and incremental encoder interface, and 20 bits of digital I/O. Finally, the Control Desk software allows one to display and store system variables and change control parameters.

Power Supplies. The specifications for the power supplies used to power the various electrical and electronic components are shown below.

Table 2.2 Power supply specifications

Power supply for	Specifications
Displacement sensor	-17.5 to -26 Vdc
Power amplifier	27 to 48 V, 7 A continuous, 9 A peak
Signal conditioning circuit	± 15 V

A block diagram of the experimental test rig is shown in Figure 2.5. A picture of the actual test rig is shown in Figure 2.6.

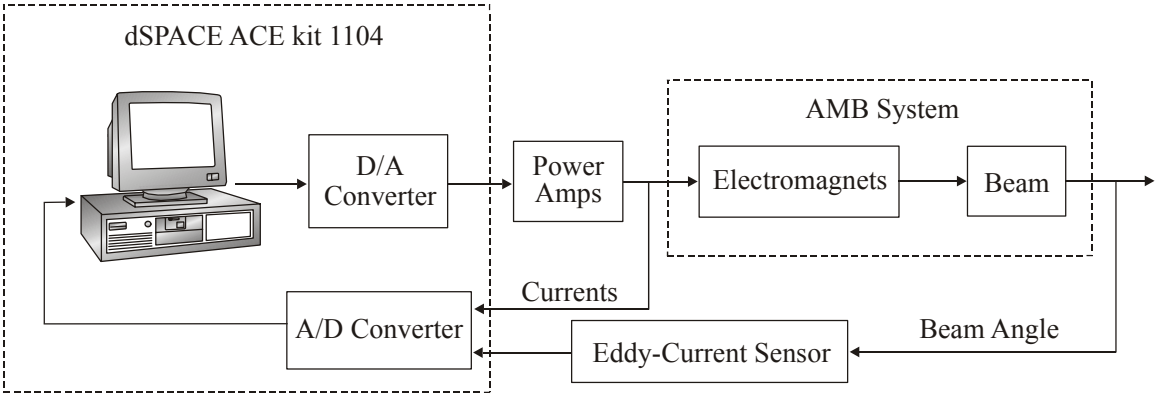

Figure 2.5: Block diagram of experimental AMB test rig

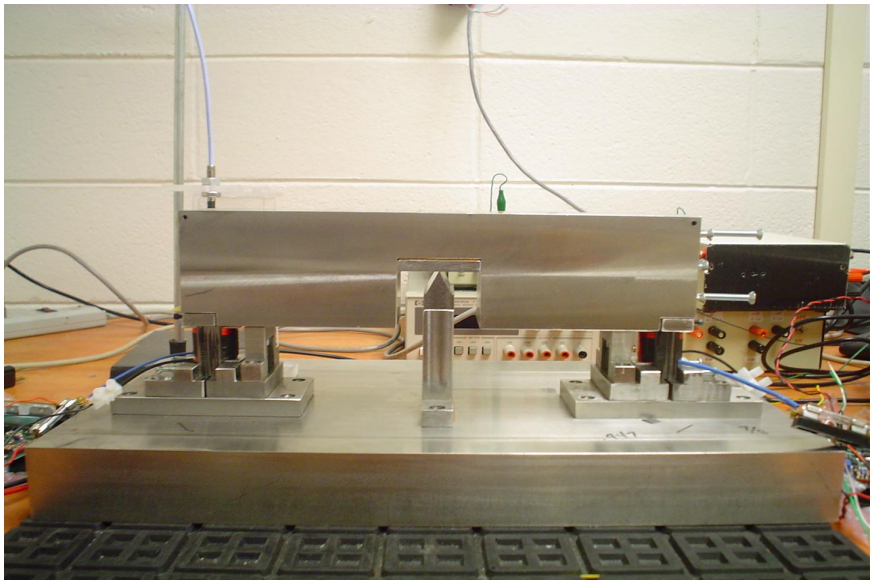

Figure 2.6: Picture of the experimental AMB test rig

Chapter 3 Smart-Bias Control Development

3.1 AMB System Model

The nonlinear electromechanical model of the experimental AMB system can be subdivided into three parts:

a. Mechanical subsystem;

b. Electromechanical coupling;

c. Electrical subsystem.

The mechanical subsystem is given by the following equation

$$\bar{J}\ddot{\theta} = \sum_{i=1}^{2} F_i(\phi_i) \quad \text{where} \quad \bar{J} = \frac{J}{L} \tag{3.1}$$

where $\theta(t)$ represents the angular position of the beam, $\phi_i(t)$ is the magnetic flux in the i^{th} electromagnet, $F_i(\phi_i)$ denotes the force produced by the i^{th} electromagnet, J is the beam's polar moment of inertia, and L is the length from the pivot to the electromagnet center line (see Figure 2.1).

The electromechanical coupling, which relates the force to the magnetic flux, is given by [8]

$$F_i = (-1)^{i+1} \frac{3\phi_i^{\,2}}{4\mu_o A} \tag{3.2}$$

where μ_o is the permeability of air and A is the cross sectional area of the electromagnet.

The electrical subsystem is governed by the following equations [8]

$$N\dot{\phi}_i + \frac{3(g_o + (-1)^i L\theta) + l}{2\mu_o AN} R_i \phi_i = v_i \qquad i = 1, 2 \tag{3.3}$$

where N denotes the number of turns of coil in the electromagnet, g_o is the nominal air gap, $l = \frac{l_{iron}}{\mu_r}$ is a constant depending upon the length of the flux path and the relative permeability, R_i is the resistance of the i^{th} electromagnet coil, and $v_i(t)$ is the voltage control input of the ith electromagnet.

In the formulation of (3.2) and (3.3), it was assumed that fringing and leakage are negligible and the magnetic circuit is linear. Under these assumptions, the relationship between the current and flux is given by

$$I_i = \frac{3(g_o + (-1)^i L\theta) + l}{2\mu_o AN}\phi_i \tag{3.4}$$

where $I_i(t)$ is the current in the i^{th} electromagnet.

The following table presents a summary of various system parameters.

Table 3.1: System parameters

Parameter	**Value**
Beam length	0.32 m
Beam mass (m)	10.0924 kg
L	0.145415 m
J	0.0983 kg-m^2
g_o	0.3302 mm
Range for θ (beam touching auxiliary stops)	{-0.0020, 0.0020} rad
N	244
R_i, i = 1,2	1.3 Ω
A	98.12 mm^2
l	7.885×10^{-5} m
μ_r	1750

3.2 Problem Statement

The control objective is threefold and can be stated as follows. Under the assumption that the beam position, beam velocity, and magnetic fluxes are measurable, design a voltage-level control law for the nonlinear AMB model represented by (3.1)-(3.3) that [11]:

i. Regulates the beam angle to zero, i.e., $\theta(t) \to 0$ as $t \to \infty$;

ii. Reduces the steady-state ohmic power loss in the coil;

iii. Contains no control singularity.

For the sake of clarity, we will revisit here most of the details the control design proposed in [11]. To facilitate the control design, we define $r(t)$ representing the weighted sum of the beam position and velocity [18]

$$r = \theta + \alpha\dot{\theta} \tag{3.5}$$

where α is a positive constant control gain. In addition, we define the flux tracking error $\eta_i(t), i = 1, 2$ as

$$\eta_i = \phi_{di} - \phi_i \tag{3.6}$$

where $\phi_{di}(t)$ represents the desired magnetic flux which is yet to be specified.

Ohmic power losses, denoted here by $P_L(t)$, have the form

$$P_L = \sum_{i=1}^{2} I_i^2 R_i \ . \tag{3.7}$$

Using (3.4), P_L can be written in the terms of magnetic flux as follows

$$P_L = \frac{1}{4(\mu_o AN)^2} \sum_{i=1}^{2} (3(g_o + (-1)^i L\theta) + l)^2 \phi_i^2 R_i \ . \tag{3.8}$$

In the steady state (i.e., when $\theta(t) = 0$), the above equation will simplify to

$$(P_L)_{ss} = \frac{(3g_o + l)^2}{4(\mu_o AN)^2} \sum_{i=1}^{2} (\phi_i^2)_{ss} R_i \tag{3.9}$$

where $(\cdot)_{ss}$ is the steady state value of the variable. It is obvious that in order to reduce $(P_L)_{ss}$, we must reduce $(\phi_{di})_{ss}$. As a result, we can restate control objective ii as to ensure that the closed-loop system operates with *zero bias flux* in the steady state.

3.3 Control Design and Analysis

The controller designed proposed in [11] is based on the integrator backstepping approach [6]. Rewriting the mechanical subsystem equation in terms of (3.5) as follows

$$\begin{aligned} \bar{J}\dot{r} &= \bar{J}\alpha\dot{\theta} + \sum_{i=1}^{2} F_i(\phi_{di}) - \sum_{i=1}^{2} (F_i(\phi_{di}) - F_i(\phi_i)) \\ &= \bar{J}\alpha\dot{\theta} + \sum_{i=1}^{2} \frac{3(-1)^{i+1}\phi_{di}^2}{4\mu_o A} - \sum_{i=1}^{2} \frac{3(-1)^{i+1}}{4\mu_o A}(\phi_{di} + \phi_i)\eta \end{aligned} \tag{3.10}$$

where the term $\sum_{i=1}^{2} F_i(\phi_{di})$ was added and subtracted to the right hand side, and then (3.2) and (3.6) were used. Based on (3.10), we design the desired flux $\phi_{di}(t)$ to satisfy the equation $\sum_{i=1}^{2} F_i(\phi_{di}) = f_d$ as follows

$$\phi_{di} = 2\frac{\sqrt{\mu_o A}}{\sqrt{3}} \sqrt{\frac{((-1)^{i+1} f_d + \sqrt{f_d^2 + \gamma_o^2})}{2}} \tag{3.11}$$

where $\gamma_o(t) \in \Re$ is a differentiable, nonnegative signal related to desired bias flux to be designed, and $f_d(t) \in \Re$ denotes the desired net force given by

$$f_d = -\bar{J}\alpha\dot{\theta} - k_m r \tag{3.12}$$

with k_m being a positive constant control gain. The closed-loop mechanical subsystem is now obtained by substituting (3.11) and (3.12) into (3.10)

$$\bar{J}\dot{r} = -k_m r - \sum_{i=1}^{2} \frac{3(-1)^{i+1}(\phi_{di} + \phi_i)\eta_i}{4\mu_o A} \tag{3.13}$$

The backstepping design procedure mandates that we now formulate the dynamics of the variable $\eta_i(t)$. Taking time derivative of (3.6), multiplying by *N*, and substituting for $N\dot{\phi}_i(t)$ from (3.3) gives

$$N\dot{\eta}_i = \Omega_i + \frac{3(g_o + (-1)^i L\theta) + l}{2\mu_o AN} R_i \phi_i - v_i \tag{3.14}$$

where the term $\Omega_i(x, \dot{x}, \phi_i, \gamma_o, \dot{\gamma}_o) \in \Re$ is defined as

$$\Omega_i = N\frac{\partial \phi_{di}}{\partial f_d}\dot{f}_d + N\frac{\partial \phi_{di}}{\partial \gamma_o}\dot{\gamma}_o. \tag{3.15}$$

Note that the partial derivatives in (3.15) can be calculated from (3.11) as follows

$$\frac{\partial \phi_{di}}{\partial f_d} = \sqrt{\frac{1}{6}}\sqrt{\frac{\mu_o A}{(-1)^{i+1} f_d + \sqrt{f_d^2 + \gamma_o^2}}}\left((-1)^{i+1} + \frac{f_d}{\sqrt{f_d^2 + \gamma_o^2}}\right) \tag{3.16}$$

$$\frac{\partial \phi_{di}}{\partial \gamma_o} = \sqrt{\frac{1}{6}}\sqrt{\frac{\mu_o A}{(-1)^{i+1} f_d + \sqrt{f_d^2 + \gamma_o^2}}}\left(\frac{\gamma_o}{\sqrt{f_d^2 + \gamma_o^2}}\right) \tag{3.17}$$

while $\dot{f}_d(t)$ can be written using (3.12) and (3.1) as follows

$$\dot{f}_d = \frac{-\bar{J}\alpha - k_m}{\bar{J}} \sum_{i=1}^{2} F_i(\phi_i) - k_m \alpha \dot{\theta}. \tag{3.18}$$

Based on the form of (3.14) and (3.13), the control input is designed as [11]

$$v_i = \Omega_i + \frac{3(g_o + (-1)^i L\theta + l)}{2\mu_o AN} R_i \phi_i + k_{ei}\eta_i - \frac{3(-1)^{i+1}}{4\mu_o A}(\phi_{di} + \phi_i) r \tag{3.19}$$

where k_{ei} is a positive constant control gain. After substituting (3.19) into (3.14), we obtain the closed-loop electrical subsystem

$$N\eta_i = -k_{ei}\eta_i + \frac{3(-1)^{i+1}}{4\mu_o A}(\phi_{di} + \phi_i)r \,. \tag{3.20}$$

To analyze the stability of the closed-loop AMB system, we use the Lyapunov function

$$V = \frac{1}{2}\bar{J}r^2 + \frac{1}{2}N\sum_{i=1}^{2}\eta_i^2 \,. \tag{3.21}$$

Note that $v(t)$ can be bounded as follows

$$\frac{1}{2}\lambda_1\|z\|^2 \le V \le \frac{1}{2}\lambda_2\|z\|^2 \tag{3.22}$$

where

$$z = [r \quad \eta_1 \quad \eta_2]^T, \qquad \lambda_1 = \min\{\bar{J}, N\}, \qquad \lambda_2 = \max\{\bar{J}, N\} \,. \tag{3.23}$$

After taking the time derivative of (3.21) and substituting the values from (3.13) and (3.20), we get

$$\dot{V} = -k_m r^2 - \sum k_{ei}\eta_i^2 \le -\lambda_3\|z\|^2 \le -\frac{2\lambda_3}{\lambda_2}V \tag{3.24}$$

where (3.22) was used and

$$\lambda_3 = \min\{k_m, k_{e1}, k_{e2}\} \,. \tag{3.25}$$

After solving the differential inequality of (3.24) [15], we can show that the state vector $z(t)$ defined in (3.23) is globally exponentially stable in the sense that

$$\|z(t)\| \le \sqrt{\frac{\lambda_2}{\lambda_1}}\|z(0)\|\exp\left(\frac{-\lambda_3}{\lambda_2}t\right) \tag{3.26}$$

where (3.22) was used. Since $\theta(t)$ is related to $r(t)$ given by (3.5), we can use standard arguments [15] to show that

$$|\theta(t)| \le \zeta_p \exp(-\sigma t) \quad \text{and} \quad |\dot{\theta}(t)| \le \zeta_v \exp(-\sigma t) \tag{3.27}$$

where ζ_p, ζ_v denote some positive constants and

$$\sigma = \min\left\{\frac{\lambda_3}{\lambda_2}, \alpha\right\}. \tag{3.28}$$

The above result proves the regulation control objective was achieved. In addition, it ensures $f_d(t)$ of (3.12) is bounded for all time. In the following section, we show how to design the desired bias flux γ_o such that all remaining closed-loop signals, including the control law of (3.19), remain bounded while reducing ohmic power losses.

3.4 Bias Design and Analysis

The controller design above ensures that $r(t)$, $\theta(t)$, $\dot{\theta}(t)$ and $\eta_i(t)$ go to zero exponentially fast; hence, we know that in the steady state, $\phi_i(t) = \phi_{di}(t)$. After substituting (3.11) into (3.9), we get

$$\begin{aligned}(P_L)_{ss} &= \frac{(3g_o + l)^2}{4(\mu_o AN)^2}\sum_{i=1}^{2}(\phi_{di}^2)_{ss} R_i \\ &= \frac{2(3g_o + l)^2}{12\mu_o AN^2}\sum_{i=1}^{2}\left((-1)^{i+1}(f_d)_{ss} + \sqrt{(f_d)_{ss}^2 + (\gamma_o)_{ss}^2}\right)R_i.\end{aligned} \tag{3.29}$$

After substituting (3.12), (3.26), and (3.27) into (3.29), we obtain

$$(P_L)_{ss} = \frac{2(3g_o + l)^2 (R_1 + R_2)}{12\mu_o AN^2}(\gamma_o)_{ss}. \tag{3.30}$$

From (3.30), it seems we could set $\gamma_o \equiv 0$ to nullify $(P_L)_{ss}$; however, this would lead to a control singularity as shown next. Note that the control voltage $v_i(t)$ in (3.19) is a function of Ω_i. Using (3.15)-(3.18), we get

$$\lim_{f_d \to 0} \Omega_i = N\sqrt{\frac{\mu_o A}{6\gamma_o}}\left[\left((-1)^{i+1} + \frac{f_d}{\sqrt{f_d^2 + \gamma_o^2}}\right)\left(\frac{-\bar{J}\alpha - k_m}{\bar{J}}\sum F_i(\phi_i) - k_m\alpha\dot{\theta}\right) + \dot{\gamma}_o\right] \tag{3.31}$$

which indicates $v_i(t)$ would blow up if $\gamma_o \equiv 0$.

In [11], the above problem was overcome by designing a *smart* bias flux. That is, γ_o was designed as a function of the beam states $\theta(t),\dot{\theta}(t)$ in a manner that reduces AMB power losses and avoids control singularities without affecting the closed-loop stability. The following theorem states the conditions that $\gamma_o\left(\theta,\dot{\theta}\right)$ should satisfy to ensure the above conditions.

Theorem 1. Let $\gamma_o(\theta,\dot{\theta})$ satisfy the following properties:

1. $\gamma_o(\theta,\dot{\theta}) \in \mathcal{L}_\infty$ *if* $\theta(t), \dot{\theta}(t) \in \mathcal{L}_\infty$;

2. $\left|\frac{\dot{\theta}}{\sqrt{\gamma_o}}\right|, \left|\frac{\ddot{\theta}}{\sqrt{\gamma_o}}\right|, \left|\frac{\frac{\partial\gamma_o}{\partial\theta}}{\sqrt{\gamma_o}}\right|, \left|\frac{\frac{\partial\gamma_o}{\partial\dot{\theta}}}{\sqrt{\gamma_o}}\right| \in \mathcal{L}_\infty$;

3. $\gamma_o(\theta,\dot{\theta}) \to 0$ if and only if $\theta(t), \dot{\theta}(t) \to 0$.

Then, the control law of (3.19) and all closed-loop signals are bounded for all time. In addition, $(P_L)_{ss} = 0$.

Proof. See [11].

Remark 1. *Property 3 of Theorem 1 is primarily motivated by the physical observation that if the rotor is perfectly centered in the bearing system (i.e.,* $\theta(t) = \dot{\theta}(t) = 0$*), then there is no need for the AMB electromagnets to apply forces on the rotor. Therefore, the electromagnets can be de-energized by turning off the bias flux. Another motivation for Property 3 is the mathematical fact that* $\gamma_o(\theta,\dot{\theta}) \to 0$ *implies* $f_d(t) \to 0$. *This avoids the scenario where* $\Omega_i \to \infty$ *as* $\gamma_o \to 0$.

The following lemma states a specific form for $\gamma_o(\theta,\dot{\theta})$ proposed in [11] to satisfy Theorem 1.

Lemma 1. Let $\gamma_o(\theta, \dot{\theta})$ be designed as

$$\gamma_o(\theta, \dot{\theta}) = \beta(\theta^2 + \dot{\theta}^2) \tag{3.32}$$

where β is some positive constant, then Theorem 1 holds.

Proof. See [11].

Chapter 4 Experimental Results

The smart-bias controller derived in Chapter 3, given by (3.19), (3.11), (3.12), and (3.32), was implemented on the experimental AMB test rig described in Chapter 2. Specifically, its performance was compared to a standard constant-bias controller (i.e., the right-hand side of (3.32) was replaced with a constant) in terms of beam stabilization, ohmic power loss, and energy dissipated.

4.1 Experimental Procedure

The experiment was conducted by releasing the beam from a non-zero angle θ. The repeatability of the initial angle was ensured by placing shims in the gap between the electromagnet and the target piece. The beam was held at rest at the initial angle, and suddenly released to initiate the experimental run. Experiments were conducted for two sets of initial conditions:

$$\theta(0) = \begin{cases} -5.2\times10^{-4} \text{ rad} \\ 5.2\times10^{-4} \text{ rad} \end{cases} \qquad \dot{\theta}(0) = 0 \text{ rad/s} \qquad \phi_1(0) = \phi_2(0) = 0 \ Wb. \tag{4.1}$$

First, the constant-bias controller was run to provide a baseline performance. The control gains were tuned by trial-and-error until the beam was successfully stabilized at $\theta \approx 0$ rad. Then, the bias constant γ_o was adjusted until we reached the smallest value possible without destabilizing the system. This procedure resulted in the following values for the control gains and bias constant

$$\alpha = 2 \qquad k_{e1} = k_{e2} = 1\times10^5 \qquad k_m = 10 \qquad \gamma_o = 0.1. \tag{4.2}$$

To evaluate the smart-bias controller, the control gains and bias multiplicative parameter β were tuned to match as close as possible the beam response obtained with the constant-bias controller. This procedure resulted in the following values for the control gains and bias parameter

$$\alpha = 3 \qquad k_{e1} = k_{e2} = 1.5 \times 10^5 \qquad k_m = 5 \qquad \beta = 2. \tag{4.3}$$

We note that both control laws were implemented without the last term on right-hand side of (3.19).

4.2 Experimental Results

In order to illustrate the effectiveness of the controllers in stabilizing the beam, we conducted an *open-loop* experiment where the beam was released from the initial angle $\theta(0) = 5.2 \times 10^{-4}$ rad with the power amplifiers turned off. Figure 4.1 shows the open-loop response for the beam angle $\theta(t)$. Notice that the beam hits the right auxiliary stop at $t \approx 0.45$ sec and eventually settles on the left auxiliary stop after $t \approx 7.0$ sec. Next, a *disturbance rejection* experiment was conducted by manually tapping on the beam endpoints during the experimental run of both controllers. The results are shown in Figure 4.2, where the sharp peaks denote the instants where the disturbance was applied. Notice how the controllers are able to re-stabilize the beam.

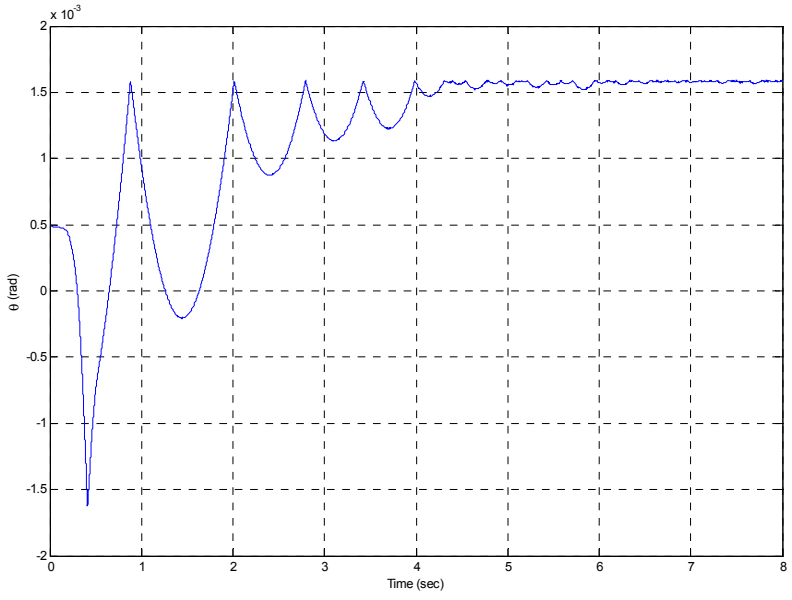

Figure 4.1: Open-loop response of $\theta(t)$

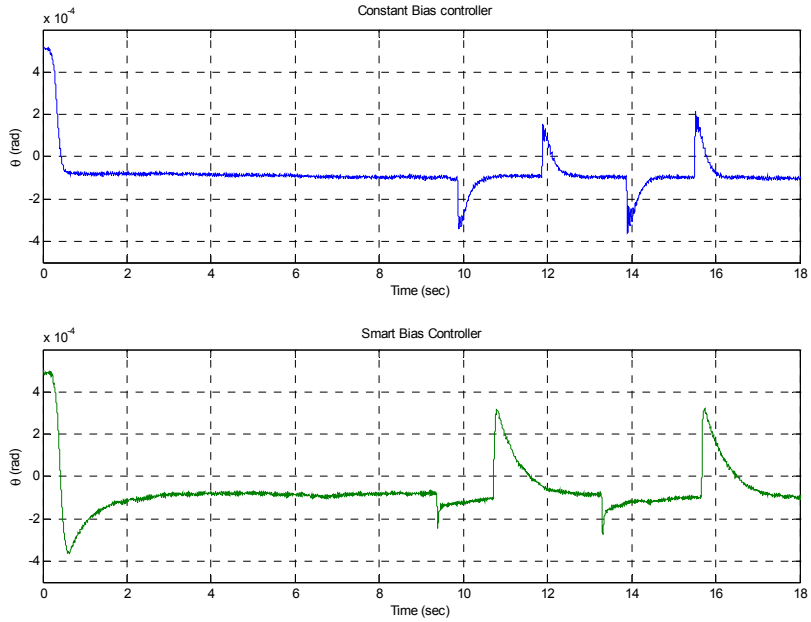

Figure 4.2: Disturbance-rejection response of $\theta(t)$

In the following plots, the subscripts 1 and 2 represent the variables of the left and right electromagnets, respectively. Figures 4.3-4.6 compare the performance of the constant-bias and smart-bias controllers with the control gains given in (4.2) and (4.3) for the case where $\theta(0) = -5.2 \times 10^{-4}$ rad. Figure 4.3 shows a slightly faster stabilization of the beam with the constant-bias controller; however, most importantly, both controllers produced the same steady-state value for the beam angle. In Figure 4.4, we see that the smart-bias controller required less current than the constant-bias controller to achieve a comparable stabilization performance. A comparison of the ohmic power loss $P_L(t)$, given by (3.7), of the two control schemes is shown in Figure 4.5. Notice that the smart-bias controller has a steady-state power loss approximately 7.5 smaller. To further assess the performance of the two controllers, we also calculated the energy dissipated by the AMB system as defined by

$$E_d = \int_0^{t_f} P_L(t)dt \tag{4.4}$$

where t_f = 7 sec was the final experiment time. The energy dissipation results are shown in Table 4.1, indicating approximately ninefold reduction in the energy dissipated with the smart-bias controller. Finally, the control voltages of both controllers are shown in Figure 4.6.

Table 4.1 Energy Dissipated for $\theta(0) = -5.2 \times 10^{-4}$ rad

Controller	E_d **(Joules)**
Constant-bias	0.0497
Smart-bias	0.0058

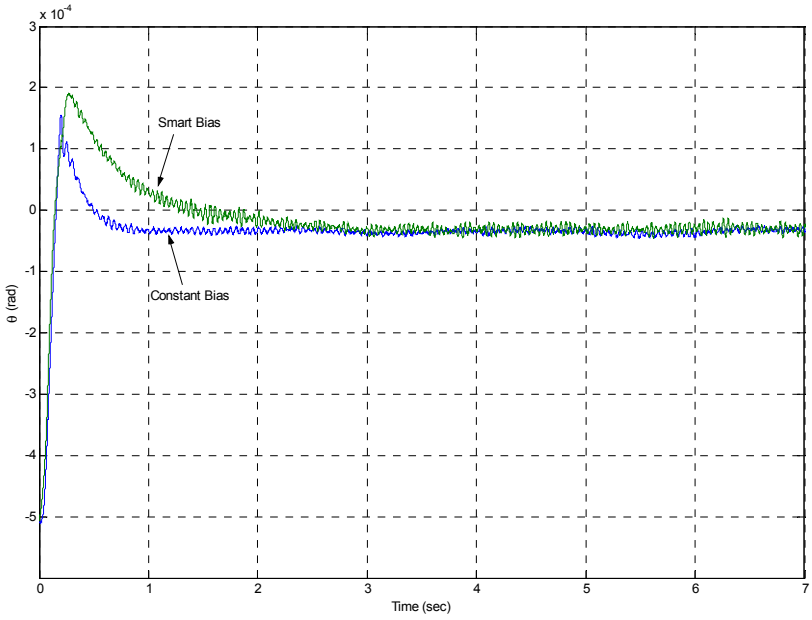

Figure 4.3: Beam angle $\theta(t)$ for $\theta(0) = -5.2 \times 10^{-4}$ rad

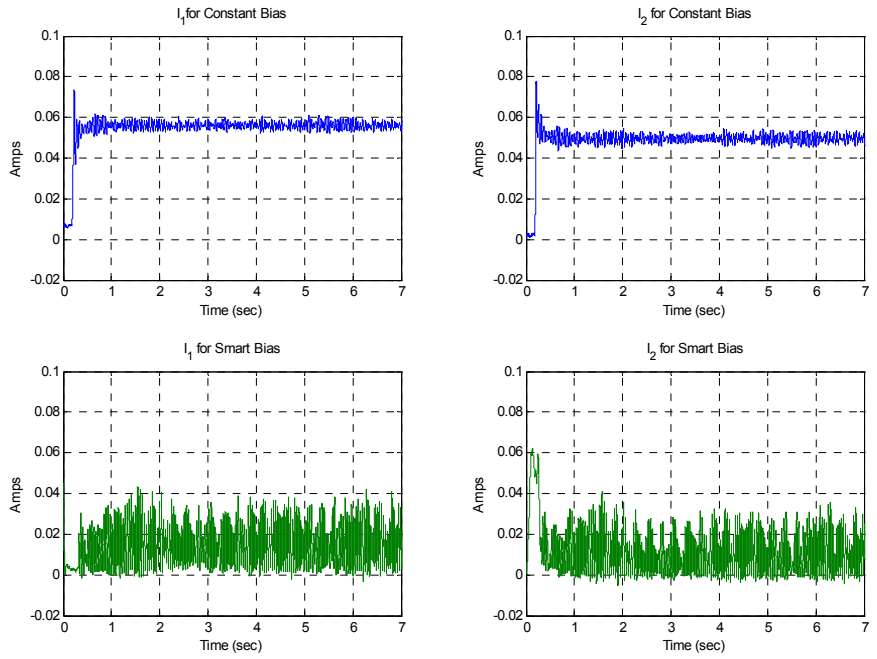

Figure 4.4: Electrical currents $I_1(t)$ and $I_2(t)$ for $\theta(0) = -5.2 \times 10^{-4}$ rad

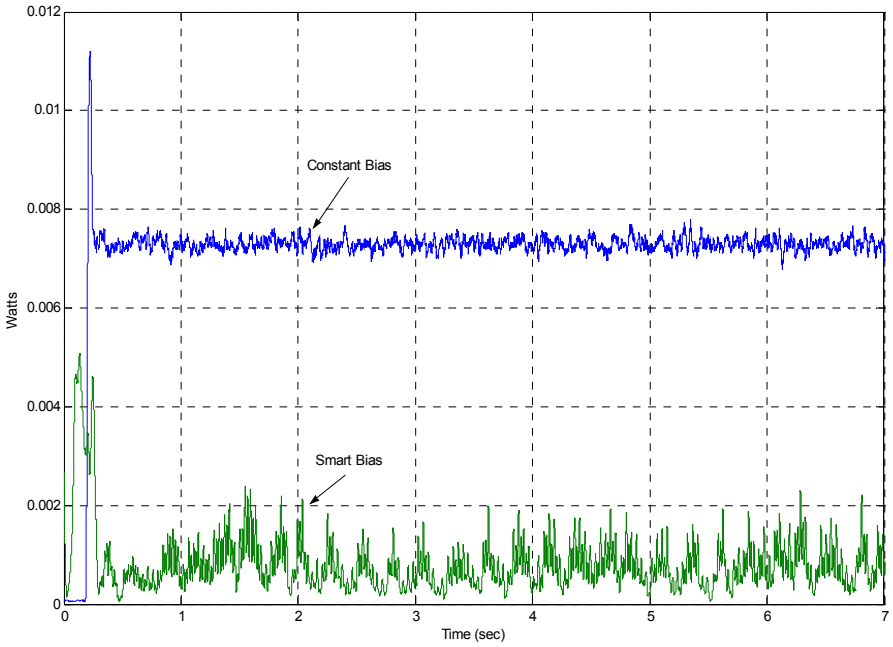

Figure 4.5: Ohmic power loss $P_L(t)$ for $\theta(0) = -5.2 \times 10^{-4}$ rad

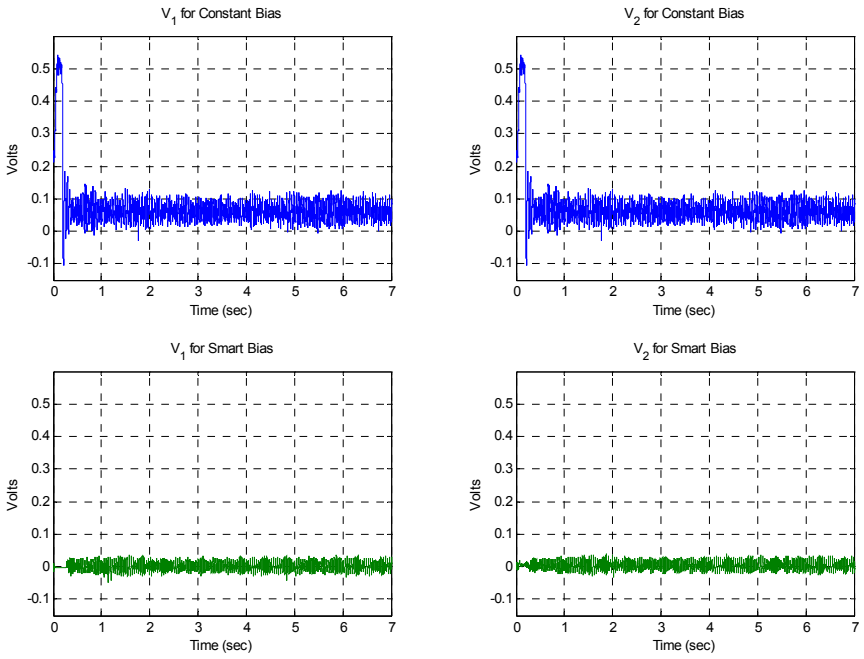

Figure 4.6: Control voltages $V_1(t)$ and $V_2(t)$ for $\theta(0) = -5.2 \times 10^{-4}$ rad

In order to qualitatively confirm the above results, a second experimental run was performed by releasing the beam from $\theta(0) = 5.2 \times 10^{-4}$ rad. The results are shown in Figures 4.7-4.10. Again, we see a comparable stabilization performance; however, the smart-bias controller had significantly less ohmic power loss as shown in Figure 4.9. The energy dissipated by both controllers, shown in Table 4.2, again indicate an approximately eightfold reduction during the 7 sec of the experimental run.

Table 4.2 Energy Dissipated for $\theta(0) = 5.2 \times 10^{-4}$ rad

Controller	E_d **(Joules)**
Constant-bias	0.0535
Smart-bias	0.0064

We note that the power loss of the smart-bias controller in the experiments did not have steady-state value of zero, as predicted by the theory, because the beam was not regulated *exactly* to zero. This happened because of sensor noise, inaccuracy in the displacement sensor calibration, and small uncertainties in various system parameters (e.g., g_o, J, l, and L). Nevertheless, the results confirm the ability of the smart-bias controller to reduce the ohmic power loss and energy dissipated in the AMB system in comparison to the constant-bias case without significantly affecting the stabilization performance.

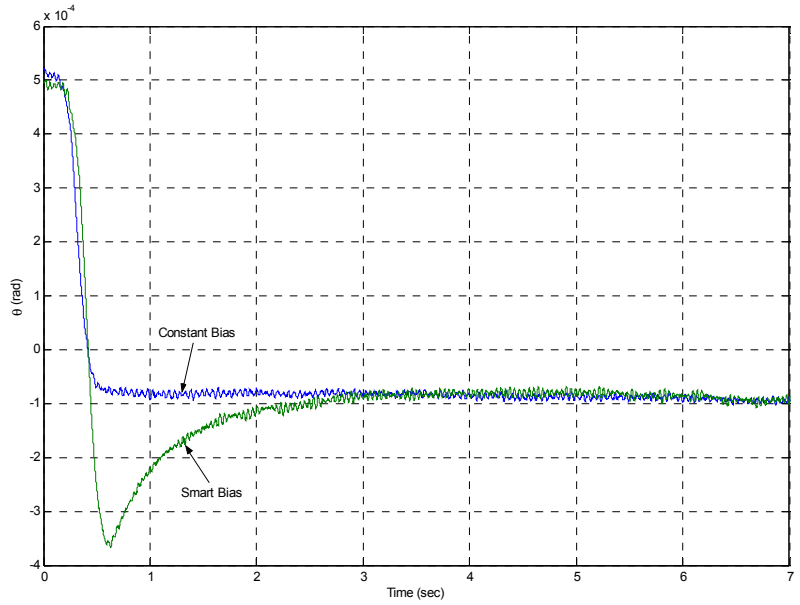

Figure 4.7: Beam angle $\theta(t)$ for $\theta(0) = 5.2 \times 10^{-4}$ rad

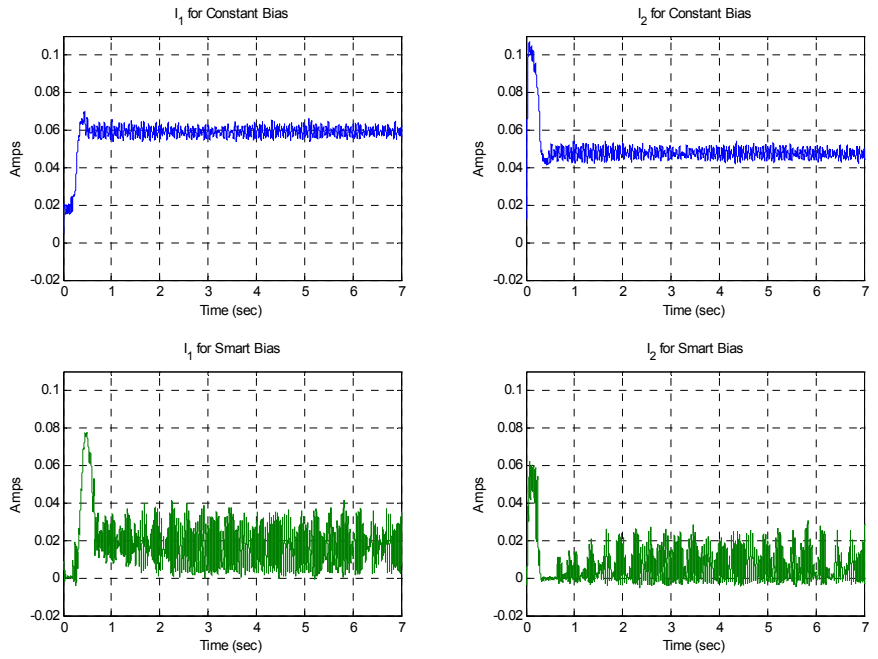

Figure 4.8: Electrical currents $I_1(t)$ and $I_2(t)$ for $\theta(0) = 5.2 \times 10^{-4}$ rad

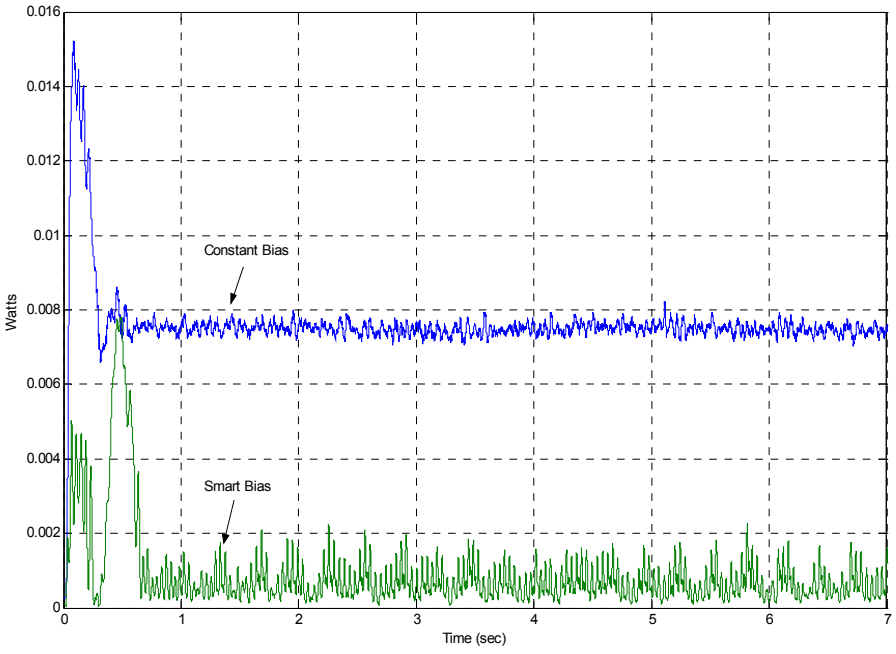

Figure 4.9: Ohmic power loss $P_L(t)$ for $\theta(0) = 5.2 \times 10^{-4}$ rad

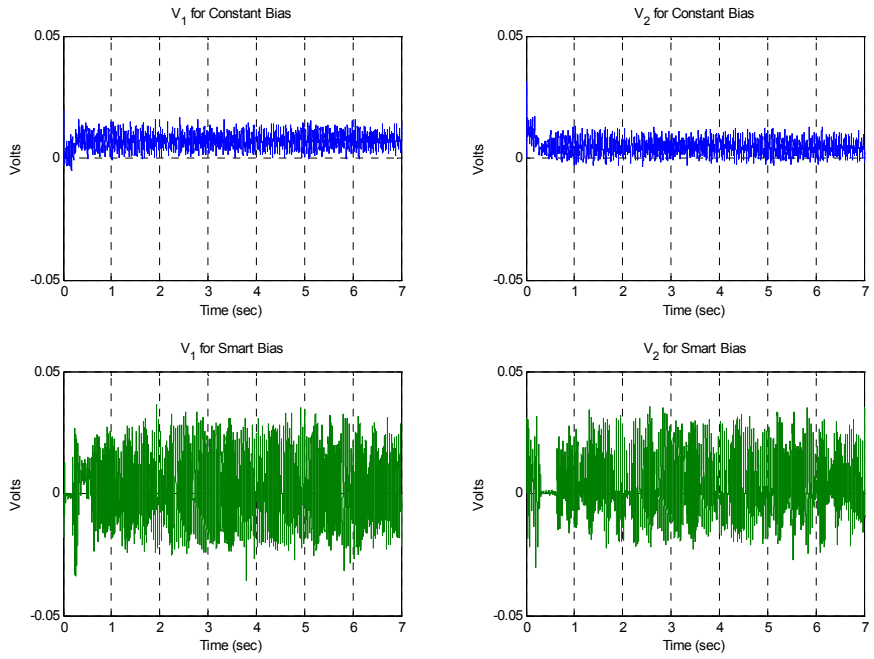

Figure 4.10: Control voltages $V_1(t)$ and $V_2(t)$ for $\theta(0) = 5.2 \times 10^{-4}$ rad

Chapter 5 Conclusions

This thesis presented an experimental validation of the new smart-bias AMB controller recently proposed in [11]. A one-DOF AMB test rig, inspired by the nonlinear control AMB benchmark experiment proposed in [8, 13], was built and used to implement the control algorithm. The experimental AMB setup is an excellent testbed for evaluating advanced AMB controllers as well as new control algorithms for nonlinear systems.

The experimental validation consisted of comparing the beam stabilization, ohmic power loss, and energy dissipated of the smart-bias controller to a standard constant-bias control law. The experimental results provided a definitive, qualitative confirmation of the theoretical and numerical results presented in [11]. Namely, that the smart-bias controller can significantly reduce electrical power losses and energy dissipated in the AMB system without affecting the rotor stabilization. Although the constant-bias controller showed a slightly faster transient behavior, we believe the transient performance of the smart-bias controller can be improved by a more refined tuning of the control gains. Improving the method of releasing the beam from the initial angle could also eliminate some of the performance discrepancy.

Bibliography

1. W.W. Anderson and C.R. Keckler, ”An Integrated Power/Attitude Control System (IPACS) for Space Application,” *Proc. 5th IFAC Symp. Automatic Control in Space*, 1973.

2. Charara and B. Caron, “Magnetic Bearings: Comparison Between Linear and Nonlinear Functioning,” *Proc. Int. Symp. Magnetic Bearings*, pp. 451-460, Alexandria, VA, Jul. 1992.

3. M. Fujita, K. Hatake, and F. Matsumura, “Loop Shaping Based Robust Control of a Magnetic Bearing,” *IEEE Control Syst. Mag*., Vol. 13, No. 4, pp. 57-65, Aug. 1993.

4. C.D. Hall, “High-Speed Flywheels for Integrated Energy Storage and Attitude Control,” *Proc. American Control Conf.*, pp. 1894-1898, Albuquerque, NM, June 1997.

5. C. Knospe and C. Yang, “Gain-Scheduled Control of a Magnetic Bearing with Low Bias Flux,” *Proc. Conf. Decision and Control*, pp. 418-423, San Diego, CA, Dec. 1997.

6. M. Krstic, I. Kanellakopoulos, and P. Kokotovic, *Nonlinear and Adaptive Control Design*, New York, NY: John Wiley & Sons, 1995.

7. J. Levine, J. Lottin, and J.C. Ponsart, “A Nonlinear Approach to the Control of Magnetic Bearings,” *IEEE Trans. Control Syst. Tech.*, Vol. 4, No. 5, pp. 524-544, Sept. 1996.

8. J.D. Lindlau, *Dynamic Force Biasing of Active Magnetic Bearings via Feedback Linearization*, M.S. thesis, University of Virginia, May 1999.

9. A.M. Mohamed and F.P. Emad, “Conical Magnetic Bearings with Radial and Thrust Control,” *IEEE Trans. Automatic Control*, Vol. 37, No. 12, pp. 1859-1868, Dec. 1992.

10. N. Motee, M.S. de Queiroz, Y. Fang, and D.M. Dawson, “Active Magnetic Bearing Control with Zero Steady-State Power Loss,” *Proc. American Control Conf.*, pp. 827-832, Anchorage, Alaska, May 2002.

11. N. Motee and M.S. de Queiroz, “Control of Active Magnetic Bearings with a Smart Bias,” *Proc. IEEE Conf. Decision and Control*, pp. 860-865, Las Vegas, NV, Dec. 2002.

12. NASA Glenn Research Center, Power and Propulsion Office, http://space-power.grc.nasa.gov/ppo/ projects/flywheel/.

13. *Proceedings of the American Control Conference*, Vols. 3 and 4, Chicago, IL, June 2000.

14. M.S. de Queiroz and D.M. Dawson, "Nonlinear Control of Active Magnetic Bearings: A Backstepping Approach," *IEEE Trans. Control Syst. Tech.*, Vol. 4, No. 5, pp. 545-552, Sept. 1996.

15. M.S. de Queiroz, D.M. Dawson, S. Nagarkatti, and F. Zhang, *Lyapunov-Based Control of Mechanical Systems*, Cambridge, MA: Birkh, 2000.

16. M.S. de Queiroz, D.M. Dawson, and H. Canbolat, "A Backstepping-Type Controller for a 6-DOF Magnetic Bearing System," *Proc. IEEE Conf. Decision and Control*, pp. 3370-3375, Kobe, Japan, Dec. 1996.

17. M.S. de Queiroz, D.M. Dawson, and A. Suri, "Nonlinear Control of a Large Gap 2-DOF Magnetic Bearing System Based on a Coupled Force Model," *IEEE Proc. - Control Theory and Appl.*, Vol. 145, No. 3, pp. 269-276, May 1998.

18. J.Slotine and W.Li, *Applied Nonlinear Control*, Englewood Cliff, NJ: Prentice Hall Co., 1991

19. P. Tsiotras and E. Velenis, "Low-Bias Control of AMB's Subject to Saturation Constraints," *Proc. IEEE Conf. Control Appl.*, pp. 138-143, Ancorage, AK, Sept. 2000.

20. P. Tsiotras, B. Wilson, and R. Bartlett, "Control of a Zero-Bias Magnetic Bearing Using Control Lyapunov Functions," *Proc. IEEE Conf. Decision and Control*, pp. 4048-4053, Sydney, Australia, Dec. 2000.

21. P. Tsiotras and M. Arcak, "Low-Bias Control of AMB Subject to Voltage Saturation: State-Feedback and Observer Designs," *Proc. IEEE Conf. Decision and Control*, pp. 2474-2479, Las Vegas, NV, 2002.

22. P. Tsiotras, H. Shen, and C. Hall, "Satellite Attitude Control and Power Tracking with Energy/Momentum Wheels," *J. Guidance, Control, and Dynamics*, Vol. 24, No. 1, pp. 23-34, Jan.-Feb. 2001.

23. C. Yang, C. Knospe, and P. Tsiotras, "Optimal Control of a Magnetic Bearing without Bias Flux using Finite Voltage," *Optimal Control Appl. and Methods*, Vol. 19, pp. 227-246, 1998.

Vita

Pradhananga, Shailesh is a native of Nepal. He was born March 6,1972. He completed his Bachelor of Science in Mechanical Engineering at Regional Institute of Technology, Jamshedpur, India, in 1996. He came to the United States in 2001 to pursue his Master of Science in Mechanical Engineering degree at Louisiana State University.

He is the elder son of Ratna and Premi Pradhananaga and has a brother and a sister.